This is a preprint, the final version is subject to change, of the American Mineralogist (MSA)
Cite as Authors (Year) Title. American Mineralogist, in press.
DOI: https://doi.org/10.2138/am-2018-6214

Revision 1

Partial melting of ultramafic granulites from Dronning Maud Land, Antarctica: constraints from melt inclusions and thermodynamic modeling

Silvio Ferrero[1,2], Gaston Godard[3], Rosaria Palmeri[4], Bernd Wunder[5], Bernardo Cesare[6]

[1]*Institut für Geowissenschaften, Universität Potsdam, Deutschland*

[2]*Museum für Naturkunde (MfN), Berlin, Deutschland*

[3]*Université Paris-Diderot, Institut de Physique du Globe de Paris, UMR CNRS 7154, Paris, France*

[4]*Museo Nazionale dell'Antartide, Università di Siena, Italia*

[5]*Helmholtz-Zentrum Potsdam, GFZ, D-14473 Potsdam, Deutschland*

[6]*Dipartimento di Geoscienze, Università di Padova, Italia*

ABSTRACT

In the Pan-African belt of the Dronning Maud Land, Antarctica, crystallized melt inclusions (nanogranitoids) occur in garnet from ultramafic granulites. The granulites contain the peak assemblage pargasite+garnet+clinopyroxene with rare relict orthopyroxene and biotite, and retrograde symplectites at contacts between garnet and amphibole. Garnet contains two generations of melt inclusions. Type 1 inclusions, interpreted as primary, are isolated, <10 μm in size, and generally have negative crystal shapes. They contain kokchetavite, kumdykolite and phlogopite, with quartz and zoisite as minor phases, and undevitrified glass was identified in one inclusion. Type 2 inclusions are <30 μm in size, secondary, and contain amphibole, feldspars, zoisite. Type 2 inclusions appear to be the crystallization products of a melt that coexisted with an immiscible CO_2-rich fluid.

The nanogranitoids were re-homogenized after heating in a piston-cylinder in a series of four experiments to investigate their composition. The conditions ranged between 900 and 950°C at 1.5–2.4 GPa. Type 1 inclusions are trachytic and ultrapotassic, whereas type 2 melts are dacitic to rhyolitic. Thermodynamic modeling of the ultramafic composition in the MnNCKFMASHTO system shows that anatexis occurred at the end of the prograde *P-T* path, between the solidus (at ca. 860°C–1.4 GPa) and the peak conditions (at ca. 960°C–1.7 GPa). The model melt composition is felsic and similar to that of type 1 inclusions, particularly when the melting degree is low (< 1 mol%), close to the solidus. However the modeling fails to reproduce the highly potassic signature of the melt and its low H_2O content. The combination of petrology, melt inclusion study and thermodynamic modeling supports the interpretation that melt was produced by anatexis of the ultramafic boudins near peak *P-T* conditions, and that type 1 inclusions contain the anatectic melt that was present during garnet growth. The felsic, ultrapotassic composition of the primary anatectic melts is compatible with low melting degrees in the presence of biotite and amphibole as reactants.

INTRODUCTION

When continents collide and/or are subducted, large volumes of crustal rocks may reach temperatures sufficiently high for partial melting to occur. Part of this material consists of metasediments and granitoids, whose behavior during melting – in terms of chemical reactions, conditions and products – has been the target of an extensive experimental campaign over three decades long (e.g., Clemens and Wall 1981; Vielzeuf and Clemens 1992; Patiño-Douce and Harris 1998; Vielzeuf and Montel 1994; Mann and Schmidt 2015; Schmidt 2015). However, continental

collision and crustal subduction does not only involve silica-rich rocks. Mafic and intermediate rocks are thought to form much of the lower crust (Rudnick and Gao 2003), whereas ultrabasic rocks, such as orogenic peridotites, may also be involved (Bodinier and Godard 2003). Like silica-rich lithologies, silica-poor rocks can reach high temperature conditions under which they will begin to melt during subduction and/or exhumation. Partial melting of intermediate and mafic rocks is known to play a key role in the formation of the first continental crust in the early Earth (e.g. Johnson et al. 2013, 2017), and has a crucial influence on chemical differentiation (Condie et al. 2003; Sizova et al. 2015). Experiments suggest that the melting of metabasalts (Beard and Lofgren 1990; Rushmer et al. 1991; Rapp et al. 1991), eclogites (Rapp et al. 2003) and amphibolites (Foley et al. 2002) can produce trondhjemite–tonalite–granodiorite (TTG) suites that form the bulk of exposed Archean continental crust (Johnson et al. 2017) as well as adakitic magmas in volcanic arc settings (Peacock et al. 1994; Rapp and Watson 1995; Quian and Hermann 2013).

Nanogranitoids – crystallized droplets of anatectic melt generally enclosed in peritectic minerals – have been so far mainly investigated in (meta)sediments and (meta)granitoids, the most common rock types in the upper-middle crust (Cesare et al. 2009; Ferrero et al. 2012; Cesare et al. 2015; Bartoli et al. 2016). Their discovery has allowed direct comparison between natural and experimental melts, and allows us to test and improve our understanding of crustal anatexis involving felsic protoliths. However, although there is a significant body of experimental work pertaining to the partial melting of mafic protoliths (e.g., Rapp and Watson 1995) no melt inclusions from eclogites have been remelted to provide a comparison with this experimental data, despite having been often reported (see compilation in Cesare et al. 2015).

Here we investigate the first reported nanogranitoids from (ultra)mafic high-*P* granulites. The inclusions occur within a pargasite–garnet–augite–bearing granofels from Dronning Maud Land in Antarctica. These inclusions are characterized via a combined approach of petrological investigation and experimental re-homogenization followed by in-situ microchemical analyses and thermodynamic modeling. Melt inclusion re-homogenization is a common technique for magmatic inclusion studies (see e.g. the review paper of Audetat and Lowenstern 2014) that has been adapted by Bartoli et al. (2013a) for the purpose of investigating melt inclusions within metamorphic rocks, using a piston-cylinder apparatus to achieve re-homogenization (see also Cesare et al. 2011; Bartoli et al. 2013b; Cesare et al. 2015; Ferrero et al. 2015, 2016a). In the present work the measured compositions of the original melt and the experimental re-homogenization conditions are then compared and integrated with the results of thermodynamic modeling based on the bulk composition of the host rock, which was performed using recently developed thermodynamic models for metabasic rocks (Green et al. 2016; Palin et al. 2016). The approach constrains the physicochemical conditions of melting of mafic systems, allowing comparison between the natural and the calculated melts. The results improve our understanding of the behavior of the mafic/ultramafic crustal rocks during high-temperature metamorphism and anatexis.

GEOLOGICAL SETTING AND SAMPLE DESCRIPTION

The samples investigated in this study are from Dronning Maud Land (DML), in East Antarctica. This region has a complex Mesoproterozoic to Paleozoic geological history age, which involves formation and disruption of Rodinia and the subsequent amalgamation of Gondwana (Jacobs 1999; Jacobs et al. 1998, 2003;

Bauer et al. 2003; Satish-Kumar et al. 2008). In paleogeographic reconstructions of Gondwana, the central DML commonly occupies a key area, representing the probable southern extension of the Mozambique belt into East Antarctica (Shackleton 1996; Jacobs et al. 1998; Jacobs 1999; Bauer et al. 2003; Elvevold and Engvik 2013). The Mozambique belt, one of the most extensive orogens in Earth's history (Holmes 1951), is interpreted as having formed during the closure of the Mozambique ocean and the subsequent collision and amalgamation of East and West Gondwana during the Pan-African orogeny (Hoffman 1991; Grunow et al. 1996; Shackleton 1996; Jacobs et al. 1998; Jacobs 1999; Bauer et al. 2003; Elvevold and Engvik 2013; Pauly et al. 2016). These tectonic events induced medium- to high-pressure metamorphism in the DML (Godard and Palmeri 2013).

Several major lithological units (Fig. 1) have been distinguished and mapped in the metamorphic basement of central DML (Paech et al. 2004). The oldest formation is a thick supracrustal pile made of a bimodal metavolcanic complex (1130 ± 12 Ma U-Pb age on zircon: Jacobs et al. 1998; Jacobs 1999) with interlayered metasedimentary rocks. This metavolcanic complex was later intruded by voluminous granite batholiths and sheet-like felsic intrusions (1086 ± 20 Ma U-Pb age on zircon:Jacobs et al. 1998; Jacobs 1999). Two younger (600–510 Ma) plutonic suites are also present in the area (Fig.1).

One of the best exposed areas of the central DML is the Conradgebirge in the Orvinfjella (Fig. 1), where four different geological formations have been distinguished (Colombo and Talarico 2004; Palmeri et al. 2017). The *metavolcanic complex* (Fig. 1) consists of amphibole-bearing gneisses, amphibolites and plagiogneisses with minor gabbros and ultramafic lenses. This complex is interleaved with rare thin belts of metasedimentary rocks (*metasedimentary complex*

in Fig. 1), mainly biotite+sillimanite+garnet±orthopyroxene gneisses, calc-silicate rocks, marbles and quartzites. The *metaplutonic complex* consists of garnet-bearing migmatitic augen orthogneisses with subordinate garnet-bearing amphibolites and granofelses. Younger (~530 Ma) hornblende-bearing orthogneisses with rare garnet+clinopyroxene amphibolites have been described in its central part (Jacobs 1999; Bauer et al. 2003). Cambrian syenites and charnockites intrude the metavolcanic complex (Post-kinematic *igneous rocks* in Fig. 1).

The complex tectono-metamorphic evolution of central DML can be best followed in the Conradgebirge (Jacobs et al. 1998; Jacobs 1999; Bauer et al. 2003). The oldest tectono-metamorphic event (D1) is assumed to be Mesoproterozoic (~1080 Ma: Jacobs et al. 1998; Jacobs 1999; Bauer et al. 2003). A later major event (D2) was responsible for the generation of the main foliation accompanying high-grade granulite-facies metamorphism, with a syntectonic migmatization dated at ca. 570 Ma that constrains D2 as part of the Pan-African orogenic cycle (Bauer et al. 2003). Deformation structures D3 and D4 are attributed to the same orogenic cycle and are coeval with the emplacement of Cambrian syenite and charnockite intrusions.

The rock investigated in this study is a garnet-bearing ultramafic rock (28-12-95TF4, hereafter TF4), which occurs as a meter-sized pod, one of a string of boudins likely derived from former ultramafic dykes within highly strained and strongly migmatized orthogneisses of the metaplutonic complex (Fig. 1; Colombo and Talarico 2004). It was sampled in December 1995 during the International GeoMaud expedition at the location 9° 41’ 41”W longitude and 71° 47’ 8”S latitude. The sample is now stored at the rock repository of Siena University’s Museo Nazionale dell’Antartide (Italy) (see the online database at //www.mna.it/collezioni/catalogo-

rocce-sede-di-siena). More information on this sample and other (ultra)mafic rocks from the same area is available in Palmeri et al. (2017).

PETROGRAPHY

The studied sample is a medium-grained granoblastic rock mainly consisting of clinoamphibole, garnet and clinopyroxene (Fig. 2a; mineral abbreviations after Kretz 1983). Porphyroblastic cm-sized garnets show a nearly homogeneous core with a plateau-shaped profile (core average: $Alm_{38}Prp_{44}Grs_{15}Sps_3$) and an abrupt X_{Fe} increase at the rims (from 80 μm onwards to the edge (up to $Alm_{54}Prp_{27}Grs_{16}Sps_3$, see Table 1 for mineral and bulk-rock compositions). The most abundant mineral is brown-green pargasitic amphibole (Al^{IV} ≈ 1.9 a.p.f.u; X_{Mg} ≈ 0.69; Table 1). Clinopyroxene is present as large, anhedral crystals, up to 5 mm in size, with widespread 10-μm-thick exsolution lamellae of orthopyroxene (X_{Mg} ≈ 0.67), plagioclase (An_{94}) and pargasitic amphibole. The pre-exsolution clinopyroxene whose original composition was estimated using EPMA scans, is a subcalcic Tschermak-rich diopside ($En_{36}Fs_{14}Wo_{29}$Ca-Ts_{15}Ca-Ti-Ts_1 Jd_3; Table 1).

Abundant symplectites are interpreted to have grown during retrogression. A kelyphite with two concentric symplectites occurs at the contacts between garnet and amphibole (Fig. 2a). The inner symplectite, replacing garnet consists of Opx+Pl+Spl±Ol (kel_1 in Fig. 2a), whereas the outer symplectite, replacing amphibole, is made of Pl+Opx±Cam_2±Spl±Ilm±Bt (kel_2 in Fig. 2a). Aluminous spinel has X_{Mg} = 0.36–0.39, plagioclase is anorthite (An_{97}) and biotite is phlogopite (X_{Mg} = 0.76–0.80). Scarce olivine (X_{Mg} = 0.53–0.54), apparently developed later in the symplectite, replacing orthopyroxene and enveloping spinel. Another symplectite made of plagioclase ($An_{90\text{-}96}$) and undeformed orthopyroxene (X_{Mg} = 0.66) developed at the

177 contacts between garnet and clinopyroxene. Retrogression is also documented by
178 Opx, Pl and Cam exsolution lamellae in Cpx (see above).

179 Apart from the targeted polycrystalline inclusions, a few, rare mineral
180 inclusions of biotite and amphibole occur in garnet and belong to the prograde phase
181 assemblage. A single mm-sized plagioclase ($An_{48–60}$) has also been observed in the
182 symplectite after garnet, and is considered as a relict formerly isolated in garnet.
183 Finally, a single kinked and resorbed orthopyroxene within the matrix (X_{Mg} = 0.70) is
184 also interpreted as a relict inherited from a previous assemblage. The polycrystalline
185 inclusions targeted in our study were found in garnet porphyroblasts belonging to the
186 metamorphic peak main assemblage.

187

188 ## STUDY METHODS

189 The polycrystalline inclusions were characterized in detail via back-scattered-
190 electron (BSE) imaging, energy-dispersive-spectrometry (EDS) elemental mapping,
191 micro-Raman spectroscopy and, after experimental re-homogenization, electron
192 probe microanalyses (EPMA). Their composition was compared with the theoretical
193 melt composition provided by thermodynamic modeling.

194

195 ### Analytical techniques

196 Inclusions from three garnet porphyroblasts have been investigated in
197 polished thin sections and in garnet chips separated from doubly-polished thick
198 sections. After investigation using a polarized-light optical microscope, a Field
199 Emission Gun electron microprobe (FEG-EMP) JEOL Hyperprobe JXA-8500F
200 (Natural History Museum, Berlin) was used to acquire high-resolution BSE images

and EDS elemental maps to identify the microstructural features of the inclusions and the phases that occur in both primary and pseudosecondary inclusions.

Micro-Raman spectroscopy has been performed on both types of inclusions using a HORIBA Jobin Yvon LabRAM HR 800 located at the Institute of Earth and Environmental Science, University of Potsdam. This machine is equipped with a Peltier-cooled multichannel CCD detector and coupled with an Olympus BX41 petrographic microscope. An air-cooled Nd:YAG laser was used for excitation (λ = 532 nm, laser power on the sample of 2–3 mW) with a grating of 300 lines/mm, slit width and confocal hole set to set to 100 μm and 200 μm, respectively. The Raman spectra of the crystal phases were acquired with a 100× objective in the wavenumber range 100–4000 cm^{-1}, integrating 3 repetitions of 60 s with spectral resolution of 10 cm^{-1}.

Inclusion homogenization

Experimental re-homogenization of the inclusions was performed on garnet chips with unexposed nanogranitoids selected from different garnets. After selection, the chips were loaded in a platinum capsule then filled with silica powder, without adding water. The capsules were kept at in a piston-cylinder apparatus under high-temperature and high-pressure conditions for 24 hours. The temperature in the capsule was controlled using a Type S thermocouple (Pt-PtRh10) with a ±10 °C uncertainty, while the accuracy of the pressure measurement is estimated to be ±0.05 GPa. Quenching of the experimental charge took place at high pressure, and the machine was unloaded only after reaching ambient temperature. In-situ analyses were then performed on capsules mounted in epoxy and polished to expose re-homogenized inclusions (for more details on the experimental procedure see Bartoli

et al. 2013b and Ferrero et al. 2015). The glass resulting from re-homogenization of 10 nanogranitoid inclusions was analyzed using a JEOL JXA-8200 EMP at Potsdam University. Analytical conditions were similar to previous studies of nanogranitoids (see e.g., Ferrero et al. 2012) at 15 kV, 3.5 nA and beam diameter of 1 μm to avoid contamination from the surrounding host.

Thermodynamic modeling

In order to evaluate the *P-T* conditions of anatexis and to model the formation of the melt preserved as inclusions in garnet, we constructed an isochemical *P-T* diagram (or *P-T* pseudosection), in the MnNCKFMASHTO system using the THERMOCALC software package (v 3.40) and the internally-consistent thermodynamic dataset of Holland and Powell (2011, release 6.2 of 2015).

The chosen chemical molar composition is that of the bulk rock (see Table 1). It was verified by least squares regression that this composition was a linear combination of sample TF4 mineral compositions (see method in Godard, 2009). The bulk O (or Fe^{3+}) content, being unknown, has been tested in the range 0.05–0.25 mol%. It has little effects on the *P-T* curves and isopleths, which are shifted of ca. 6°C or 0.05 GPa for the investigated range. The effect is greater when spinel is involved, at low pressures, because of its noticeable content in Fe^{3+}. Since the Spl+Gt+Opx+Pl-bearing assemblages that correspond to the kelyphite formed around garnet during retrogression do not appear for values greater than 0.09 mol%, a value of 0.08 mol% has been selected. H_2O saturation was assumed. The following activity-composition models were used: melt (in the NCKFMASH system), clinoamphibole (NCKFMASHTO) and calcic augite (NCFMASO) by Green et al. (2016); garnet (MnCFMASO), orthopyroxene (MnCFMASO), biotite (MnKFMASHO)

and ilmenite (FMTO) by White et al. (2014a, 2014b); spinel (FMATO) by White et al. (2002); and, ternary plagioclase (NCKAS) by Holland and Powell (2003). We are aware that we are using the melt model of Green et al. (2016) out of its pressure range of calibration (i.e. P < 1.3 GPa), and that the estimated melt compositions should be considered with care, in particular the H_2O content. As a consequence we have adopted the constraint of H_2O saturation in the modelling, and will not discuss the modelled melt H_2O contents. Since THERMOCALC allows calculation of the modal abundance of the melt and its composition in the CNKFMASH system, molar compositions have been converted into weight % of oxides on an anhydrous basis, in order to allow comparison only of the major element model melt compositions with those of the natural melt inclusions (Table 4).

RESULTS

Microstructures of inclusions

Two types of inclusions have been distinguished based on their microstructural distribution in the garnet porphyroblasts of the investigated rock. The first type (type 1 hereafter) shows a sporadic and random distribution in the large anhedral garnet porphyroblasts, supporting the interpretation that inclusions were trapped during garnet growth, i.e. they are primary according to the classification of Roedder (1984). Type 1 inclusions are generally <10 μm in diameter, isolated, and only rarely do they occur in clusters (Figs 2b,c), a spatial distribution often observed to be characteristic of primary nanogranitoids (Cesare et al. 2015). Type 1 inclusions generally have isometric shapes (Figs. 2d), although some clusters contain abundant parallel tubular inclusions, <40 μm in length (Fig. 2e). Under BSE observation, they commonly display a well-developed negative-crystal shape (Fig. 2f).

Inclusions of the second type (type 2) can be distinguished from type 1 because they are arranged along planes and trails cross-cutting the entire crystal (Fig. 2g). As these trails are not visible in the phases adjacent to the garnet, type 2 are interpreted as of secondary nature, i.e. resulting from partial healing of microcracks (Roedder 1984) likely formed shortly after garnet growth, thus postdating the formation of type 1 inclusions and predating the formation of kelyphite. Type 2 inclusions include both polycrystalline and fluid inclusions, all of which occur in the same trails. The fluid inclusions are monophase at room temperature (Fig. 2h). Polycrystalline inclusions (i.e. nanogranitoids) are more abundant than fluid inclusions, and both fluid and melt inclusions are generally larger, ≤30 μm in size, than type 1 inclusions (Fig. 2g).

Phase identification

The phase assemblages of both inclusion types were characterized by BSE imaging (Fig. 3), EDS elemental mapping (Fig. 4) and micro-Raman spectroscopy (Fig. 5). Type 1 inclusions all contain an assemblage of kokchetavite, kumdykolite, phlogopite and minor quartz (Fig. 3a,b). Kokchetavite and kumdykolite are relatively rare polymorphs of K-feldspar and albite respectively, recently reported as common phases in nanogranitoids from felsic granulites (Ferrero et al. 2016). In the investigated samples kumdykolite shows characteristic Raman peaks at 492, 218 and 156 cm^{-1} (Fig. 5a) consistent with those reported in literature (Hwang et al. 2009; Kotkova et al. 2014; Ferrero et al. 2016). Kokchetavite shows Raman peaks at 392, 109 and 835 cm^{-1}, also in agreement with spectra reported by Hwang et al. (2004) and Ferrero et al. (2016). Orthopyroxene and needles of apatite are present as accessory minerals in type 1 inclusions and as tiny mineral inclusions in the

surrounding garnet host. Zoisite occurs very rarely within the melt inclusions. A single inclusion of fresh undevitrified glass has been identified among type 1 inclusions (Fig. 3d), and its amorphous nature verified by micro-Raman spectroscopy. Type 2 nanogranitoids mainly contain amphibole, feldspar and zoisite, with accessory orthopyroxene. Fluid inclusions in the same inclusion trails contain a CO_2-rich fluid (bands at 1282, 1386 cm^{-1} in Fig. 5b), with abundant N_2 (2331 cm^{-1}), minor CH_4 (2916 cm^{-1}) and rare graphite (1580 cm^{-1}; Fig. 5b). A similar COHN fluid is occasionally observed within larger nanogranitoids. Magnesite, graphite, orthopyroxene and halite (the latter identified only via EDS because Raman inactive) may occur as accessories in both polycrystalline and fluid inclusions in trails.

Melt compositions

Re-homogenization experiments were performed on portions of garnet containing both types of inclusions. The experimental charges were kept at T = 900–950 °C under a confining pressure in the range 1.5–2.4 GPa for 24 hours (Table 2). Temperature and pressure of remelting experiments reproduce the conditions at which type 1 inclusions were trapped during garnet growth, based on previous literature on the area (see e.g. Godard and Palmeri 2013). In these experiments, both type 1 and type 2 inclusions remelted into a homogeneous phase at 950°C (Fig. 6), while at 900°C they showed incomplete melting and persistence of solids together with a melt phase.

EPMA were performed on the completely re-homogenized inclusions from the runs at 950 °C, after having verified their glassy nature by means of Raman spectroscopy (Fig. 6). EMP investigation shows that the two inclusion types have very distinct compositions, defining two chemical clusters that do not overlap (Fig. 7;

Table 3). Type 1 inclusions host a hydrous alkaline glass, rich in K_2O (average 8.5 wt%) and highly potassic (K_2O / Na_2O = 3.55). Importantly the unique preserved glassy inclusion within garnet shares the same chemical features as the re-melted type 1 inclusions (Table 3). The composition of type 1 melts plots in the trachyte field of TAS classification (Fig. 7a) and in the granite field of the An-Ab-Or CIPW normative triangle (O'Connor 1965; Fig. 7b; compare with Bartoli et al. 2016). The melts are weakly peraluminous (ASI = 1.12) and have an inferred volatile content lower than 3 wt% (estimated by difference of EMPA totals from 100, with all Fe recalculated as FeO; see Table 3), most likely due to the presence of H_2O in the glass, as confirmed by micro-Raman spectroscopy (see Fig. 6a). Tiny crystals of orthopyroxene were observed within the re-homogenized glass of two inclusions and are interpreted as crystals trapped during inclusion formation. Type 2 inclusions re-homogenize to a subalkaline dacitic-rhyolitic melt (tonalite to Qtz-monzonite in the An-Ab-Or normative classification), and are slightly more peraluminous (ASI = 1.17), higher in CaO and much lower in K_2O (average K_2O = 1.70 wt%) compared to type 1 melts. The inferred volatile component, with an average of 13 wt%, is significantly higher in type 2 than in type 1 inclusions. This is supported by the much greater intensity of the asymmetric H_2O band in the region 3200–3600 cm^{-1} of the spectra acquired on re-homogenized glasses (Fig. 6b).

Thermodynamic Modeling

A pseudosection was calculated between 0.0 and 2.0 GPa and 800 to 1000 °C using the composition of sample TF4 (Table 1; in mol%): $[SiO_2]_{45.20}$ $[Al_2O_3]_{9.39}$ $[TiO_2]_{0.76}$ $[MgO]_{20.90}$ $[FeO]_{10.94}$ $[MnO]_{0.16}$ $[CaO]_{10.97}$ $[Na_2O]_{1.03}$ $[K_2O]_{0.57}$ $O_{0.08}$. The result is shown in Figure 8. The main features of interest for this work are the

location of the solidus (thick line in Fig. 8) between 870 and 950 °C depending on the pressure conditions, and the absence of orthopyroxene at pressure exceeding 1.0–1.5 GPa depending on temperature.

From this pseudosection, together with the thermodynamic modeling of 3 microdomains of the same sample, Palmeri et al. (2017) deduced a *P-T* path (Fig. 8a). The peak (at ca. 960°C–1.7 GPa: Fig. 8a) is mainly constrained by the garnet isopleth (X_{Fe} = Fe/[Mg+Fe] = 0.490 ± 0.005: Fig. 8b) that corresponds to the flat zoning pattern of the garnet porphyroblasts, which should be due to diffusive re-equilibration at high temperature. Caddick et al. (2010) have indeed demonstrated that the growth zoning of a cm-sized garnet totally resets within 0.6 Ma at 900°C. The compositions of amphibole and augite, as well as X_{Ca} of garnet, predicted by the model at the peak show a fairly good match with those measured (Palmeri et al. 2017). The main discrepancy involves X_{Fe} of amphibole and may reflect retrograde Fe-Mg diffusion during cooling and decompression.

The phase assemblage inferred to be stable close to the peak of metamorphism includes garnet, augite and amphibole, which are abundant in the matrix. In addition, the occurrence of type 1 inclusions, of primary origin and thus formed during garnet growth, indicates that melt was present and anatexis was taking place in the rock. The occurrence of small inclusions of biotite in the garnet hosting type 1 melt inclusions suggests that biotite was also present. The assemblage stable during melting was thus the orthopyroxene-free paragenesis Cam+Grt+Cpx+Bt+Liq(+Rt) that occupies a wide field in the high-grade part of the pseudosection at T > 860°C and P > 1.2 GPa.

The retrograde evolution is documented by unkinked orthopyroxene that occurs as coronas. The increase in X_{Fe} up to 0.64 observed at the rims of the garnet

crystals is also explained by this evolution, as shown by the retrograde *P-T* path that intersects the X_{Fe} garnet isopleths (Fig. 8a). Opx-An-Spl-bearing symplectites at contacts between garnet and amphibole (i.e., kelyphite), as well as orthopyroxene, clinoamphibole and plagioclase exsolution lamellae formed within augite during retrogression, indicate a final evolution towards the Grt-free Opx-Pl-Spl-bearing fields that occur at low-*P* (<0.5 GPa) and medium-*T* conditions (Fig. 8a). Further details on the *P-T* evolution of the rock are provided in Palmeri et al. (2017).

Type 1 nanogranitoids have SiO_2 and Al_2O_3 contents similar to those of the calculated melts formed close to the solidus curve (Fig. 8b,c,d; Table 4), where the amount of partial melt produced is very low (<1 mol%; e.g., 1 or 13 versus "type 1" in Table 4). This fact points toward the formation of the type 1 melt at ca. 870–890°C and 1.5 GPa.

DISCUSSION

Nature of the inclusions

Primary type 1 inclusions occur in garnets from granulite facies ultramafic boudins from the DML. Their microchemical investigation and successful experimental re-homogenization confirm that these inclusions are nanogranitoids (see Cesare et al. 2015), i.e., droplets of an original felsic melt that subsequently crystallized during cooling. The original melted nature of these multiphase inclusions is supported by the identification of one glassy inclusion occurring in the same microstructural setting and showing the same composition as the remelted type 1 inclusions. The preservation of glass within inclusions has also been reported in slowly cooled migmatites (Cesare et al. 2009). This finding widens the spectrum of rock types in which nanogranitoid studies can be applied to characterize partial melts

in natural samples. While primary melt inclusions have been recognized in numerous partially melted metasedimentary, metagranitoids and metabasic rocks (see Cesare et al. 2015), the present study is the first to report such inclusions, and to succeed in remelting them, in a rock of ultramafic composition. Type 2 inclusions display very different microstructures, which point to a secondary origin. This implies that the entrapment of inclusions postdates – of an undetermined time lag – the formation of the garnet host and thus the main melting event. As our investigation focus on the peak partial melting event, the following discussion is focused mainly on the primary type 1 inclusions.

Since the microstructural occurrence of type 1 inclusions suggests they are primary, i.e., were trapped by garnet during its growth, we can confidently conclude that garnet grew in the presence of an anatectic melt. As garnet growth implies an increase of pressure (see garnet isomodes in Fig. 8a), anatexis is likely to have occurred at the end of the prograde evolution, between the solidus and the metamorphic peak (see *P-T* path in Fig. 8a). The formation of garnet as a result of partial melting reactions is commonly observed in melting experiments involving fluid-absent melting of OH-bearing phases, e.g. biotite in sedimentary (Le Breton and Thompson 1987; Vielzeuf and Clemens 1991; Vielzeuf and Montel 1994), and amphibole in mafic rocks (Sen and Dunn 1994; Qian and Hermann 2013). Garnet production during melting, coupled with the presence of rare biotite as mineral inclusions in nanogranitoids-bearing garnets, suggest that the partial melting reaction could have involved the consumption of biotite and amphibole as OH-bearing phases. The amount of water measured in the melt (ca. 3 wt% H_2O) is consistent H_2O–undersaturated melting at the calculated *P-T* conditions anatexis (see experiments of Holtz et al. 2001).

426

427 **Polymorphs as crystallization products of trapped melt**

428 The mineral phases in type 1 nanogranitoids are consistent with the
429 crystallization of a silica-rich melt. Polymorphs of albite and K-feldspar, kumdykolite
430 and kokchetavite respectively, are common in this inclusion type. These phases
431 were first identified in diamond-bearing rocks from the Kokchetav Massif (Hwang et
432 al. 2001; 2009) and the Bohemian Massif (Kotkova et al. 2014; Perraki et al. 2014),
433 within multiphase inclusions hosted in garnet and omphacite. Ferrero et al. (2016)
434 then reported their occurrence together with glass and cristobalite in nanogranitoids
435 trapped under high-*P* conditions in diamond- and coesite-free felsic granulites from
436 the northwestern portion of the Bohemian Massif, in the Polish Sudetes. Ferrero et
437 al. (2016) constrained the formation of polymorphs as crystallization products of the
438 trapped melt at pressure below 2.0 GPa. Although no data are available on the
439 thermodynamic properties and stability fields of these phases, the petrographic
440 constraints provided by studies of the polymorph-bearing nanogranitoids, combined
441 with their lower density with respect to their most common counterparts, suggest that
442 the ultrahigh-*P* conditions deemed by some authors to be necessary for their
443 formation are not required (see discussion in Ferrero et al. 2016b). On the contrary,
444 pressure is likely to play no role in their formation, as kokchetavite was synthesized
445 at atmospheric pressure by dehydrating K-cymrite at 500°C (Kanzaki et al. 2012),
446 and the Ca-rich equivalent of kumdykolite, sviatoslawite, was observed to form in
447 material from burning dumps that experienced temperatures of ~1000°C at
448 atmospheric pressure (Chesnokov et al. 1989). However kumdykolite has not yet
449 been produced experimentally. Recently kumdykolite and kokchetavite were

identified in other nanogranitoids trapped under low-*P* conditions (Ferrero & Angel, in preparation) further excluding that pressure may be influential to their formation.

While their formation appears to be independent of both *P* and *T*, petrographic evidence suggests that these polymorphs are highly metastable, and prone to change into their more stable counterparts in the case of inclusion decrepitation (Ferrero et al. 2016b). Hence these phases can be considered as indicators that the nanogranitoids in which they occur are compositionally intact – including their volatile contents. Their composition after experimental re-homogenization is therefore representative of the melt originally trapped in the growing garnet (Ferrero et al. 2016b).

Possible origins of anatectic melts

An outcome of the present study is the Si- and K-rich character of the melt trapped in type 1 inclusions, quite unexpected since the host rock has an ultramafic composition and a low K_2O content (0.87 wt%: Table 1). Potassium-rich, Na-poor melts are not uncommon in partial melting experiments on silica-poor protoliths, but are generally less silicic, and (much) richer in MgO, reaching lamproitic composition. Wendlandt e Eggler (1980) showed that their ultrapotassic character is generally related to the presence of phlogopite in the source rocks, whereas in its absence (e.g., Rapp and Watson 1995; Sen and Dunn 1994) K_2O seldom exceeds 4 wt%. These melts are very different from those of type 1 inclusions. However, more recent experimental studies on phlogopite-bearing systems relate more closely to the compositions of melts determined in this work. One is the study of phase relations of a mafic durbachite performed by Parat et al. (2010) where melt compositions similar to type 1 inclusions are found in equilibrium with olivine, phlogopite and

clinopyroxene at 0.2 GPa and 1000°C. At higher pressure (1 GPa), experiments performed by Condamine and Médard (2014) on a phlogopite-bearing mantle composition show that melt compositions with >6 wt% K_2O in equilibrium with olivine, orthopyroxene, spinel and phlogopite can be produced from a harzburgitic protolith at 1150°C. This work highlights the positive correlation between K_2O and SiO_2, which are in turn an inverse function of the melt proportion and temperature. It follows that extrapolation of the compositional trends from Condamine and Médard (2014) to lower melt fraction is able to reproduce the melts in type 1 inclusions.

Since the above experimental works were conducted at pressures ≤1 GPa, garnet has never been found as part of the suprasolidus assemblage in equilibrium with the ultrapotassic melt. However, based on the compositional trends for melts as a function of pressure defined by Rapp and Watson (1995), we can reasonably assume that the change to garnet-bearing assemblages should not radically affect melt compositions in terms of major elements. Therefore we can conclude that, in agreement with the occurrence of biotite inclusions in garnet from sample TF4, the felsic ultrapotassic melts type 1 nanogranitoids can have originated locally through low degrees of melting of a phlogopite-bearing (ultra)mafic rock.

Even though an internal origin is plausible, we cannot rule out an external derivation for type 1 melts. In this second scenario, the boudins could have behaved as an open system and melt percolated from the adjacent orthogneisses, which show evidence of migmatization (Colombo and Talarico 2004). However, there is no evidence of melt infiltration in the matrix surrounding the garnet, since the sample does not show any crosscutting veins. Furthermore, in order to be trapped as primary inclusions in garnet, the melt would have had to percolate exactly at the time when garnet was growing. The simultaneous occurrence of these two processes is

not impossible, but it appears an unnecessary complexity, since a single process, i.e., partial melting, can generate both melt and the encasing mineral (see e.g. examples in Cesare et al. 2015).

Concerning the origin of type 2 melt, this generation of inclusions cannot be unequivocally related to a particular stage of the rock evolution because it occurs within partially healed cracks indicating a secondary origin. Such melt may result from the possible interactions of type 1 melt with an external CO_2-rich fluid and the surrounding rock, or it could even be completely unrelated in case of an exotic origin for type 2 melt. Both type 1 and type 2 melts must have been trapped at temperature conditions close to each other, as both nanogranitoids types re-homogenize at the same experimental conditions. The simultaneous presence of a silicate melt and an immiscible CO_2-rich fluid was already reported in other case studies of preserved anatectic melt inclusions (Cesare et al. 2007; Ferrero et al. 2011, 2014, 2016a).

Constraining the melting process through modeling

The thermodynamic modeling allows us to unravel the melting processes that have affected the studied ultramafic rock. As shown in Table 4 and Figure 8, the solution model for mafic melts provides a reasonable approximation of the effective composition of the primary type 1 melt inclusions, at least for low degrees of partial melting (e.g., 1, 6 and 13 in Table 4). However, the model melt composition is variable within a certain range and depends on several parameters.

The main parameters are indeed the pressure and temperature of melting, which have the main effect on the melt composition and mode (Fig. 8) but are difficult to settle with accuracy. Other parameters may have some control on the melt composition. We have investigated each of them independently, constraining the *P-T*

conditions along the *P*-*T* path of Figure 8a. The results of these tests are tabulated in Table 4.

Degree of partial melting. When the partial melt percentage is lowered, by approaching the solidus (e.g., from 5 to 1 in Table 4), the composition of modeled liquid gets closer to that of the type 1 melt inclusions, suggesting that the latter formed under a very low degree of partial melting (<1 mol% of melt). This occurs in the *P*-*T* field around 1.5–1.7 GPa and 860–890°C, where the melt isomodes are widely spaced (Fig. 8a), so that large *T* increments result in little increases of melting degree.

Bulk composition. Some liquid could have been extracted from the rock, whose actual bulk composition might not exactly represent the original system. If so, the liquid trapped in garnet was produced by the melting of a rock slightly different in composition. We have tested the plausibility of this hypothesis by modeling the liquid produced by the rock after reintegration of small quantities of melt (see White et al. 2004). We have used 4 theoretical bulk-rock compositions (6–10 in Table 4), ranging from (1.00×TF4 + 0.00×MI) to (0.97×TF4 + 0.03×MI), where TF4 and MI are the compositions (in wt%) of the whole rock and type 1 melt inclusions, respectively. At same *P* and *T*, the reintroduction of some melt in the bulk composition does not have a strong effect on the composition of the melt itself (8 versus 9 in Table 4). On the other hand, it shifts the solidus towards lower temperatures, which has some interesting consequences: (a) at the same *P* and *T*, the melt percentage increases with the quantity of reintroduced melt (compare 6 versus 7 and 8 versus 9 and 10, in Table 4); (b) shifting the solidus towards lower *T* allows the formation of melts whose composition, given by the extrapolation at lower *T* of the melt isopleths of Figure 8, is closer to that of type 1 inclusions (e.g., 10 versus “Type 1” in Table 4).

H_2O saturation. Saturation in H_2O has been assumed while constructing the *P-T* pseudosection of Figure 8 (see methodology section). Such assumption is plausible in view of the abundance of amphibole in the rock and an H_2O amount close to the saturation value was necessary to reproduce melting under realistic conditions, i.e. T<1000°C. Our calculations show that lowering the H_2O amount under the saturation value results in a shift towards higher *T* of both the solidus and melt isopleths (not shown). The consequence is that higher temperatures should be reached to produce a melt similar to type 1 inclusions (e.g. 13 in Table 4).

The minimum calculated melting temperatures, along the solidus curve and the *P-T* path in Fig. 8, are somewhat lower than those observed during experimental re-homogenization (950 ± 10°C). Experiments at 900°C only show incomplete melting of the nanogranitoids, suggesting the latter value is close to the real minimum melting temperature of the investigated melt; incomplete melting may be due to the slow kinetics of the experimental melting process inside the inclusion.

The above tests conducted independently allow conclusions to be drawn about the effects of the investigated parameters: in order to provide the best match between model and nature, the type 1 liquid should have formed at a low degree of partial melting, i.e. slightly beyond the solidus curve in the Cam+Grt+Cpx+Bt+Liq(+Rt) field of Figure 8. However, the solidus and thus the melting conditions may have shifted slightly either to lower or higher *T*, depending on the initial bulk-rock composition, the amount of H_2O and the accuracy of the melt model.

By adjusting the above parameters properly, the model provides a fair approximation of the type 1 melt composition (e.g., 10–12 and 15 versus Type 1 in Table 4). However, significant deviations occur between modeled and measured

melts (Table 4), with respect to K_2O (K_2O_{model} << K_2O_{Type1}), Na_2O (Na_2O_{Type1} < Na_2O_{model}) and, to a lesser degree, CaO (CaO_{Type1} < CaO_{model}).

One reason for these deviations could be a secondary evolution of the melt inclusions. The melt trapped in inclusions might have changed in composition after being entrapped in the host garnet. This hypothesis is however unlikely, since after entrapment the inclusions are chemically-isolated systems, sheltered with respect to the changes in the surrounding rock (Ferrero et al. 2012) unless extensive decrepitation occurs, with the formation of cracks connecting the trapped melt with the surrounding matrix (Ferrero et al. 2016b). This is not visible in the investigated inclusions, and evidence of partially-healed cracks intersecting type 1 inclusions, e.g. heterogeneities in garnet compositions, is absent; it is also in agreement with the preservation of kumdykolite and kokchetavite within inclusions. Chemical exchange of the trapped melt with garnet is also unlikely, since garnet has a constrained and alkali-free stoichiometry, and no chemical zonation is observed in the host garnet in the vicinity of the inclusions.

The second reason concerns the model used for melt (Green et al. 2016). Since it was designed for partial melting of plagioclase-bearing metabasites and includes molten Ab, An and Kfs as solution end-members, it could be not fully suitable for the almost feldspar-free studied rock, in particular with respect to the alkalis. The coexistence in our model of a small quantity of biotite with melt at temperatures as high as 1000°C (Fig. 8) seems to support this hypothesis. When the total melting of biotite is forced in the model by imposing the biotite-free assemblage Cam+Grt+Cpx+Liq(+Rt) at high *T*, the ensuing calculated melt fits better with the measured melt with respect to the alkalis (see 14 in Table 4).

IMPLICATIONS and CONCLUSIONS

- This study documents the first occurrence of primary melt inclusions in garnet from metamorphosed (ultra)mafic rocks. The felsic, ultrapotassic character of the melts is consistent with low degrees of melting of a biotite-bearing ultramafic source, in agreement with experimental evidence. Thus our finding has relevance for better constraining the genesis and composition of ultrapotassic mantle melts.
- Phase equilibria modelling indicates that the melt hosted in primary inclusions formed slightly beyond the solidus curve at 1.5–1.7 GPa and 860–890°C, and corresponds to a low degree of partial melting (<1 mol%). These *P-T* conditions of melt formation are broadly consistent with the conditions at which re-homogenization was achieved by experimental means.
- The melt preserved in the primary inclusions is close in composition to those resulting from both experiments and thermodynamic calculations, although it differs significantly in K_2O, Na_2O and CaO from the latter.
- Petrographic constraints and the low H_2O, high-K character of the type 1 melt suggest that melt production involved biotite and amphibole consumption under fluid-absent conditions.
- Melt inclusions in metamorphic rocks can contain unexpected metastable phases like glass and feldspar polymorphs, which are otherwise completely absent in the rest of the rock.

The discovery of these inclusions in silica-poor rocks opens up a new research avenue for the investigation of melting processes involving mafic/ultramafic systems, allowing petrologists to unravel the physico-chemical conditions under which melting processes affect such rocks, starting from small droplets of natural melt.

ACKNOWLEDGEMENTS

The research was realized with the financial support by *Programma Nazionale Ricerche in Antartide* (PNRA; PdR 13/B2.07), the Alexander von Humboldt Foundation, the German Federal Ministry for Education and Research and the *Deutsche Forschungsgemeinschaft* (Projects FE 1527/2-1 & FE 1527/2-2). The TF4 rock sample investigated in this study was selected from the collection available at the PNRA rock repository located at the *Museo Nazionale dell'Antartide* (Siena, Italy). F. Talarico collected the sample during the 1995-96 GeoMaud Antarctic expedition, with the logistic support of the *Bundesanstalt für Geowissenschaften und Rohstoffe* (BGR, Hannover, Germany). We are also grateful to M. Ziemann, C. Günther and P. Czaja for the assistance during analytical sessions. The authors wish to thank A. Peccerillo for petrogenetic advise, and T. Johnson and T. Rushmer for their detailed reviews which improved the quality of the paper and A. Acosta-Vigil for his careful editorial handling.

REFERENCES

Bartoli, O., Acosta-Vigil, A., Ferrero, S., and Cesare, B. (2016) Granitoid magmas preserved as melt inclusions in high-grade metamorphic rocks. American Mineralogist, 101, 1543–1559.

Bartoli, O., Cesare, B., Poli, S., Acosta-Vigil, A., Esposito, R., Turina, A., Bodnar, R.J., Angel, R.J., and Hunter, J. (2013a) Nanogranite inclusions in migmatitic garnet: Behavior during piston cylinder re-melting experiments. Geofluids, 13, 405–420.

Bartoli, O., Cesare, B., Poli, S., Bodnar, R.J., Acosta-Vigil, A., Frezzotti, M.L., and Meli, S. (2013b) Recovering the composition of melt and the fluid regime at the onset of crustal anatexis and S-type granite formation. Geology, 41, 115–118.

Bauer, W., Thomas, R.J., and Jacobs, J. (2003) Proterozoic-Cambrian history of Dronning Maud Land in the context of Gondwana assembly. In M. Yoshida, B.F. Windley and S. Dasgupta, Eds, Proterozoic East Gondwana: supercontinent assembly and breakup. Geological Society of London, Special Publications, 206, 247–269.

Caddick, M.J., Konopásek, J., Thompson, A.B. (2010). Preservation of garnet growth zoning and the duration of prograde metamorphism. Journal of Petrology, 51, 2327–2347.

Cesare, B., Ferrero, S., Salvioli-Mariani, E., Pedron, D., Cavallo, A. (2009). Nanogranite and glassy inclusions: the anatectic melt in migmatites and granulites. Geology, 37, 627-630.

Cesare, B., Acosta-Vigil, A., Ferrero S., Bartoli, O. (2011). Melt inclusions in migmatites and granulites. In: The Science of Microstructure – Part II. (eds): M.A. Forster and J.D. Fitz Gerald, Journal of Virtual Explorer, 38, paper 2, Electronic edition.

Cesare, B., Acosta-Vigil, A., Bartoli, O., and Ferrero, S. (2015) What can we learn from melt inclusions in migmatites and granulites? Lithos, 239, 186–216.

Chesnokov, B.V., Lotova, E.V., Pavlyuchenko, V.S., Usova, L.V., Bushmakin, A.F., and Nishanbayev, T.P. (1989) Svyatoslavite $CaAl_2Si_2O_8$: (orthorhombic) – A new mineral. Zapiski Vsesoyuznogo Mineralogicheskogo Obshchestva [Proceedings of the Russian Mineralogical Society] 118, 111–114 (in Russian).

Colombo, F., and Talarico, F.M. (2004) Regional metamorphism in the high-grade basement of central Dronning Maud Land, East Antarctica. In H.J. Paech, Ed., International GeoMaud Expedition of the BGR to central Dronning Maud Land in 1995-96. Geologisches Jahrhuch, B96, 7–47.

Condamine, P., and Médard, E. (2014) Experimental melting of phlogopite –bearing mantle ay 1 GPa: Implications for potassic magmatism. Earth and Planetary Science Letters, 397, 80-92.

Condie, K. C. Incompatible element ratios in oceanic basalts and komatiites: tracking deep mantle sources and continental growth rates with time. Geochemistry Geophysics Geosystems, 4, 1–28.

Elvevold, S., and Engvik, A.K., (2013) Pan-African decompressional P-T path recorded by granulites from central Dronning Maud Land. Mineralogy and Petrology, 107, 651–664.

Ferrero, S., Bartoli, O., Cesare, B., Salvioli-Mariani, E., Acosta-Vigil, A., Cavallo, A., Groppo, C., and Battiston, S. (2012) Microstructures of melt inclusions in anatectic metasedimentary rocks. Journal of Metamorphic Geology, 30, 303–322.

Ferrero, S., Bodnar, R.J., Cesare, B., and Viti, C. (2011) Re-equilibration of primary fluid inclusions in peritectic garnet from metapelitic enclaves, El Hoyazo, Spain. Lithos, 124, 117–131.

Ferrero, S., Braga, R., Berkesi, M., Cesare, B., and Laridhi Ouazaa, N. (2014) Production of metaluminous melt during fluid-present anatexis: an example from the Maghrebian basement, La Galite Archipelago, central Mediterranean. Journal of Metamorphic Geology, 32, 209–225.

Ferrero, S., Wunder, B., Walczak, K, O´Brien, P.J., and Ziemann, M. (2015) Preserved near-UHP melt from continental crust subducted to mantle depths. Geology, 43, 447-450.

Ferrero, S., Wunder, B., Ziemann, Wälle, M., and O'Brien, P.J. (2016a) Carbonatitic and granitic melts produced under conditions of primary immiscibility during anatexis in the lower crust. Earth Planetary Science Letters, 454, 121–131.

Ferrero, S., Ziemann, M.A., Angel, R.J., O'Brien, P.J. and Wunder, P.J. (2016b) Kumdykolite, kokchetavite, and cristobalite crystallized in nanogranites from felsic granulites, Orlica Snieznik Dome (Bohemian Massif): not evidence for ultrahigh pressure conditions. Contributions to Mineralogy and Petrology, 171, 3.

Foley, S., Tiepolo, M. & Vannucci, R (2002). Growth of early continental crust controlled by melting of amphibolite in subduction zones. Nature 417, 837–840.

Frost, B.R., Barnes, C.G., Collins, W.J., Arculus, R.J., Ellis, D.J., and Frost, C.D. (2001) A geochemical classification for granitic rocks. Journal of Petrology, 42, 2033–2048.

Godard, G. (2009). Two orogenic cycles in eclogite-facies gneisses of the Southern Armorican Massif (France). European Journal of Mineralogy, 21, 1173-1190.

Godard, G., and Palmeri, R. (2013) High-pressure metamorphism in Antarctica from Proterozoic to Cenozoic: a review and some geodynamic consequences. Gondwana Research, 23, 844–864.

Green, E.C.R., White, R.W., Diener, J.F.A., Powell, R., Holland, T.J.B., and Palin, R.M. (2016) Activity-composition relations for the calculation of partial melting equilibria in metabasic rocks. Journal of Metamorphic Geology, 34, 845–869.

Grunow, A., Hanson, R., and Wilson, T. (1996) Were aspects of Pan-African deformation linked to Iapetus opening? Geology, 24, 1063–1066.

Hawthorne, F.C., Oberti, R., Harlow, G.E., Maresch, W.V., Martin, R.F., Schumacher, J.C., and Welsch, M.D. (2012) Nomenclature of the amphibole supergroup. American Mineralogist, 97, 2031–2048.

Hoffman, P.F. (1991) Did the breakout of Laurentia turn Gondwanaland inside out? Science, 252, 1409–1412.

Holland, T.J.B., and Powell, R. (2003) Activity-composition relations for phases in petrological calculations: an asymmetric multicomponent formulation. Contributions to Mineralogy and Petrology, 145, 492–501.

Holland, T.J.B., and Powell, R. (2011) An improved and extended internally-consistent thermodynamic dataset for phases of petrological interest, involving a new equation of state for solids. Journal of Metamorphic Geology, 29, 333–383.

Holmes, A. (1951) The sequence of Precambrian orogenic belts in south and central Africa. 28th International Geological Congress, London 1948, 14, 254–269.

Holtz, F., Johannes, W., Tamic, N. and Behrens, H. (2001). Maximum and minimum water contents of granitic melts generated in the crust: a re-evaluation and implications. Lithos, 56, 1–14.

Hwang, S-L., Shen, P., Chu, H-T., Yui, T-F, Liou, J-G., and Sobolev, N.V. (2009) Kumdykolite, an orthorhombic polymorph of albite, from the Kokchetav ultrahigh-pressure massif, Kazakhstan. European Journal of Mineralogy, 21, 1325–1334.

Hwang, S-L., Shen, P., Chu, H-T., Yui, T-F, Liou, J-G., Sobolev, N.V., Zhang, R.Y., Shatsky, V.S., and Zayachkovsky, A.A. (2004) Kokchetavite: a new polymorph of $KAlSi_3O_8$ from the Kokchetav UHP terrain. Contributions to Mineralogy and Petrology, 148: 380–389.

Jacobs, J. (1999) NeoProterozoic/lower Palaeozoic events in central Dronning Maud Land (East Antarctica). Gondwana Research, 2, 473–480.

Jacobs, J., Fanning, C.M., and Bauer, W. (2003) Timing of Grenville-age vs. Pan-African medium-to-high grade metamorphism in western Dronning Maud Land (East Antarctica) and significance for correlations in Rodinia and Gondwana. Precambrian Research, 125, 1–20.

Jacobs, J., Fanning, C.M., Henjes-Kunst, F., Olesh, M., and Paech, H.J. (1998) Continuation of the Mozambique Belt into East Antarctica: Grenville-age metamorphism and polyphaser Pan-African high-grade events in central Dronning Maud Land. Journal of Geology, 106, 385–406.

Johannes, W., and Holtz, F. (1996) Petrogenesis and Experimental Petrology of Granitic Rocks, 335 p. Berlin, Springer.

Johnson, T. E., Brown, M., Kaus, B. J. P. & VanTongeren, J. A. Delamination and recycling of Archaean crust caused by gravitational instabilities. Nature Geoscience, 7, 47–52.

Johnson, T.E., Brown, M., Gardiner, N.J., Kirkland, C.L. & Smithies, R.H. (2017). Earth's first stable continents did not form by subduction. Nature, 543, 239–242

Kanzaki, M., Xue, X., Amalberti, J., Zhang, Q. (2012) Raman and NMR spectroscopic characterization of high-pressure K-cymrite ($KAlSi_3O_8$ H_2O) and its anhydrous form (kokchetavite). Journal of Mineralogical and Petrological Sciences, 107, 114–119.

Kotková, J., Škoda, R., and Machovič, V. (2014) Kumdykolite from the ultrahigh-pressure granulite of the Bohemian Massif. American Mineralogist, 99, 1798–1801.

Kretz, R. (1983) Symbols for rock-forming minerals. American Mineralogist, 68, 277–279.

Le Breton, N., and Thompson, A.B. (1988) Fluid-absent (dehydration) melting of biotite in metapelites in the early stages of crustal anatexis. Contributions to Mineralogy and Petrology, 99, 226–237.

Mikhno, A.O., Schmidt, U., Korsakov, A.V. (2013) Origin of K-cymrite and kokchetavite in the polyphase mineral inclusions from Kokchetav UHP calc-silicate rocks: evidence from confocal Raman imaging European Journal of Mineralogy, 25: 807–816.

O'Connor, J.T. (1965) A classification for quartz-rich igneous rocks based on feldspar ratios. U.S. Geological Survey Professional Paper, 525, 79–84.

Paech, H.J., Jacobs, J., Bauer, W., Mikhalsky, E., Talarico, F., Colombo, F., Roland, N.W., and Henjes-Kunst, F. (2004) Explanatory notes to the 1:500000 geological map of central Dronning Maud Land. In H.J. Paech H.J., Ed., International GeoMaud Expedition of the BGR to central Dronning Maud Land in 1995-96. Geologisches Jahrhuch, B96, 499 p.

Palin, R.M., White, R.W., Green, E.C.R., Diener, J.F.A., Powell, R., and Holland, T.J.B. (2016) High-grade metamorphism and partial melting of basic and intermediate rocks. Journal of Metamorphic Geology, 34, 871–892.

Palmeri, R., Godard, G., Di Vincenzo, G., Sandroni, S., and Talarico, F.M. (2017) High-pressure granulite facies metamorphism in central Dronning Maud Land (Antarctica): implications for Gondwana assembly. Lithos, under revision.

Parat, R., Holtz, F., René, M. and Almeev, R. (2010) Experimental constraints on ultrapotassic magmatism from the Bohemian Massif (durbachite series, Czech Republic). Contributions to Mineralogy and Petrology, 159, 331-347.

Pauly, J., Marschall, H.R., Meyer, H.P., Chatterjee, N., and Monteleone, B. (2016) Prolonged Ediacaran-Cambrian metamorphic history and short-lived high-pressure granulite-facies metamorphism in the H.U. Sverdrupfjella, Dronning Maud Land /East Antarctica): evidence for continental collision during Gondwana assembly. Journal of Petrology, 57, 185–228.

Perraki, M., and Faryad, S.W. (2014) First finding of microdiamond, coesite and other UHP phases in felsic granulites in the Moldanubian Zone: Implications for deep subduction and a revised geodynamic model for Variscan Orogeny in the Bohemian Massif. Lithos, 202–203, 157–166

Quian, Q., and Hermann, J. (2013) Partial melting of lower crust at 10–15 kbar: constraints on adakite and TTG formation. Contributions to Mineralogy and Petrology, 165, 1195–1224.

Rapp, R.P., Watson, E.B. (1995) Dehydration melting of metabasalt at 8–32 kbar: implications for continental growth and crust-mantle recycling. Journal of Petrology, 36, 891–931.

Rudnick, R.L., and Gao, S. (2014) Composition of the Continental Crust. In R.L. Rudnick Ed., Treatise on Geochemistry, 2nd ed., 1–51.

Rushmer, T. (1991) Partial melting of two amphibolites: contrasting experimental results under fluid-absent conditions. Contributions to Mineralogy and Petrology, 107, 41-59.

Satish-Kumar, M., Hokada, T., Kawakami, T., and Dunkley, D.J. (2008) Geosciences research in East Antarctica (0°-60°E): present status and future perspectives. In M. Satish-Kumar,Y. Motoyoshi, Y. Osanai, Y. Hiroi and K. Shiraishi, Eds., Geodynamic evolution of East Antarctica: a key to the East-West Gondwana connection. Geological Society of London, Special Publication, 308, 1–20.

Sen, C., and Dunn, T. (1994) Dehydration melting of a basaltic composition amphibolite at 1.5 and 2.0 GPa: implications for the origin of adakites. Contributions to Mineralogy and Petrology, 117, 394–409.

Shackleton, R.M. (1996) The final collision zone between East and West Gondwana. Where is it? Journal of African Earth Sciences, 23, 271–287.

Sizova, E., Gerya, T., Stüwe, K. & Brown, M. (2015). Generation of felsic crust in the Archean: a geodynamic modeling perspective. Precambrian Research, 271, 198–224.

Wendlandt, R.F., and Eggler, D.H. (1980) The origin of potassic magmas 2. Stability of phlogopite in natural spinel lherzolite and in the system $KAlSiO_4$-MgO-SiO_2-H_2O-CO_2 at high pressures and high temperatures. American Journal of Science, 280, 421-458.

White, R.W., Powell, R., and Clarke, G.L. (2002) The interpretation of reaction textures in Fe-rich metapelitic granulites of the Musgrave Block, central Australia: constraints from mineral equilibria calculations in the system K_2O-FeO-MgO-Al_2O_3-SiO_2-H_2O-TiO_2-Fe_2O_3. Journal of Metamorphic Geology, 20, 41–55.

White, R.W., Powell, R., and Halpin, J.A., 2004. Spatially-focussed melt formation in aluminous metapelites from Broken Hill, Australia. Journal of Metamorphic Geology, 22, 825–845

White, R.W., Powell, R., and Johnson, T.E. (2014a) The effect of Mn on mineral stability in metapelites revisited: new a-x relations for manganese-bearing minerals. Journal of Metamorphic Geology, 32, 809–828.

White, R.W., Powell, R., Holland, T.J.B., and Worley, B.A. (2000) The effect of TiO_2 and Fe_2O_3 on metapelitic assemblages at greenschist and amphibolite facies conditions: mineral equilibria calculations in the system K_2O-FeO-MgO-Al_2O_3-SiO_2-H_2O-TiO_2-Fe_2O_3. Journal of Metamorphic Geology, 18, 497–511.

White, R.W., Powell, R., Holland, T.J.B., Johnson, T.E., and Green, E.C.R. (2014b). New mineral activity-composition relations for thermodynamic calculations in metapelitic systems. Journal of Metamorphic Geology, 32, 261–286.

Captions

Figure 1. Detailed geological map of the Conradgebirge **(a)**. Abbreviations in the inset map of central DML: A: Annandagstoppane, B: Belgica Mountains, HF: Heimefrontfjella, KV: Kirwanveggen, SR: Sør Rondane. All topographical names are according to the Composite Gazetteer of Antarctica and given in their original form without translation (https://data.aad.gov.au/aadc/gaz/scar/).

Figure 2. Microstructural features of the investigated samples (red circles= primary inclusions). **(a)** main phase assemblage and kelyphite of TF4 sample, Back-scattered electrons (BSE) image; Cam: clinoamphibole (pargasite); Grt: garnet; Cpx: clinopyroxene with exsolution lamellae (Opx, Pl, Cam); kel_1 + kel_2: kelyphite (i.e., symplectite) developed at the contacts between garnet and amphibole; kel_1: inner kelyphite after garnet, made of Opx (light grey), Spl (bright grey), An-rich Pl (dark grey); kel_2: outer kelyphite after clinoamphibole, consisting of An-rich Pl (dark grey), Cam2 (medium grey), Opx (light grey) and minor Spl; **(b)** photomicrograph of garnet porphyroblast with primary inclusions (red circle) and pseudosecondary cracks (red arrows); **(c)** appearance of primary inclusions as clusters; **(d)** typical appearance of isometric nanogranitoids in plane-polarized light (left) and crossed polarizers (right); **(e)** elongated nanogranitoids; **(f)** pseudosecondary trails of nanogranitoids and fluid inclusions, under plane-polarized light (left) and crossed polarizers (right).

Figure 3. Back-scattered electrons (BSE) images of type 1 **(a, b)** and type 2 inclusions **(c)**; **(d)** preserved glassy inclusion.

838 **Figure 4.** Elemental EDS X-ray maps of the nanogranitoid of Figure 3a.

839

840 **Figure 5.** Raman spectra of the phases of interest identified in type 1 nanogranitoids
841 **(a)** and type 2 fluid inclusions **(b)**.

842

843 **Figure 6.** Raman spectra of re-homogenized inclusions. The amount of H_2O
844 dissolved in the glass, visible in the band 3200–3600 cm^{-1}, is much higher in type 2
845 inclusions, consistently with the EMP analyses of the glasses. The apparent
846 dishomogeneity in the host garnet visible in the lower part of the inclusion is an
847 artifact of the BSE imaging due to presence of an edge between inclusion and host.

848

849

850 **Figure 7.** Composition of analyzed nanogranitoids in **(a)** Total Alkali vs. Silica
851 diagram; **(b)** normative Ab-Or-An ternary diagram; **(c)** modified alkali-lime index
852 (MALI = $Na_2O + K_2O – CaO$) vs. SiO_2 (wt%) after Frost et al. (2001); **(d)** normative
853 Ab-Or-Qtz ternary diagram, with minimum melting curves (dashed curves) for the
854 haplogranite system at a_{H2O}=0.5 at 1.0 GPa from Johannes and Holtz (1996).

855

856 **Figure 8:** *P-T* pseudosections of the investigated sample. See the text for complete
857 information on the modeling method. The **Liquid and garnet isomodes (a)** are
858 expressed as molar percentages of compositions normalized to one element; the
859 same isomodes expressed as volume percentages would have higher (liquid) and
860 lower (garnet) values. The **P-T path (a)** takes into consideration the modeling of
861 several microdomains in the rock (Palmeri et al. 2017). The **Liquid isopleths (b–d)**
862 are expressed in recasted anhydrous wt% of oxides. **Garnet isopleths (b)**: X_{Fe} Grt =

Fe/(Fe+Mg) in garnet. **Field labels (a)**: phases are listed in order of decreasing abundance; rutile and/or ilmenite may be present in negligible amounts (see the dashed curves Rt+ and Ilm+); 1: Cam Opx Cpx Grt Spl; 2: Cam Opx Cpx Pl Grt Spl; 3: Cam Grt Opx Cpx Pl Liq; 4: Cam Opx Cpx Grt Liq Pl Spl; 5: Cam Opx Cpx Liq Grt Spl. An aqueous fluid phase is always present.

Tables

Table 1. Electron Microprobe analyses of the main crystalline phases and bulk rock composition. Amphibole: average of 24 spot analyses; Fe^{3+} is the minimal value for which the occupancy of the various sites is correct. Clinopyroxene: bulk composition of a crystal with Cam+Pl+Opx exsolution lamellae; it was obtained at the EMPA by averaging 500 analyses of contiguous areas (15 μm × 15 μm) scanned by the electron beam during data acquisition. Garnet: average of 8 spot analyses from the plateau-shaped core of a single garnet crystal. *: estimated by stoichiometry; n.d.: not determined.

Table 2. Results of piston cylinder experiments, with experimental parameters. Both inclusion types show the same behavior during each re-heating experiment.

Table 3. Melt inclusion compositions analyzed via EMP after experimental re-homogenization (see also Fig. 7).

Table 4. Model melt compositions, as a function of melting conditions. Chosen *P* and *T* belong to the estimated prograde *P-T* path (see Fig. 8a). MI: Average compositions of type 1 melt inclusions (Table 2), normalized to 100 wt% anhydrous; Model: model melt (see text); (1): mol% of the H_2O saturation value; (2): TF4 and MI

888 are bulk-rock (Table 1) and type 1 melt (Table 2) compositions, respectively; (3):
889 one-element-based mol% of melt.

890

This is a preprint, the final version is subject to change, of the American Mineralogist (MSA)
Cite as Authors (Year) Title. American Mineralogist, in press.
DOI: https://doi.org/10.2138/am-2018-6214

891

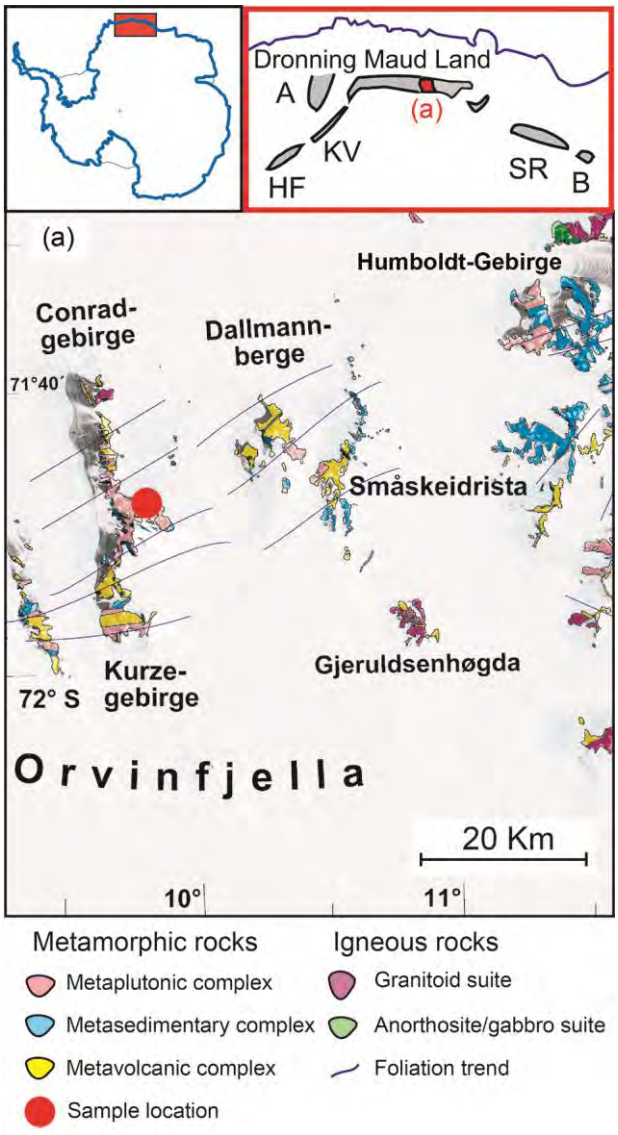

892

893 Fig. 1

894

This is a preprint, the final version is subject to change, of the American Mineralogist (MSA)
Cite as Authors (Year) Title. American Mineralogist, in press.
DOI: https://doi.org/10.2138/am-2018-6214

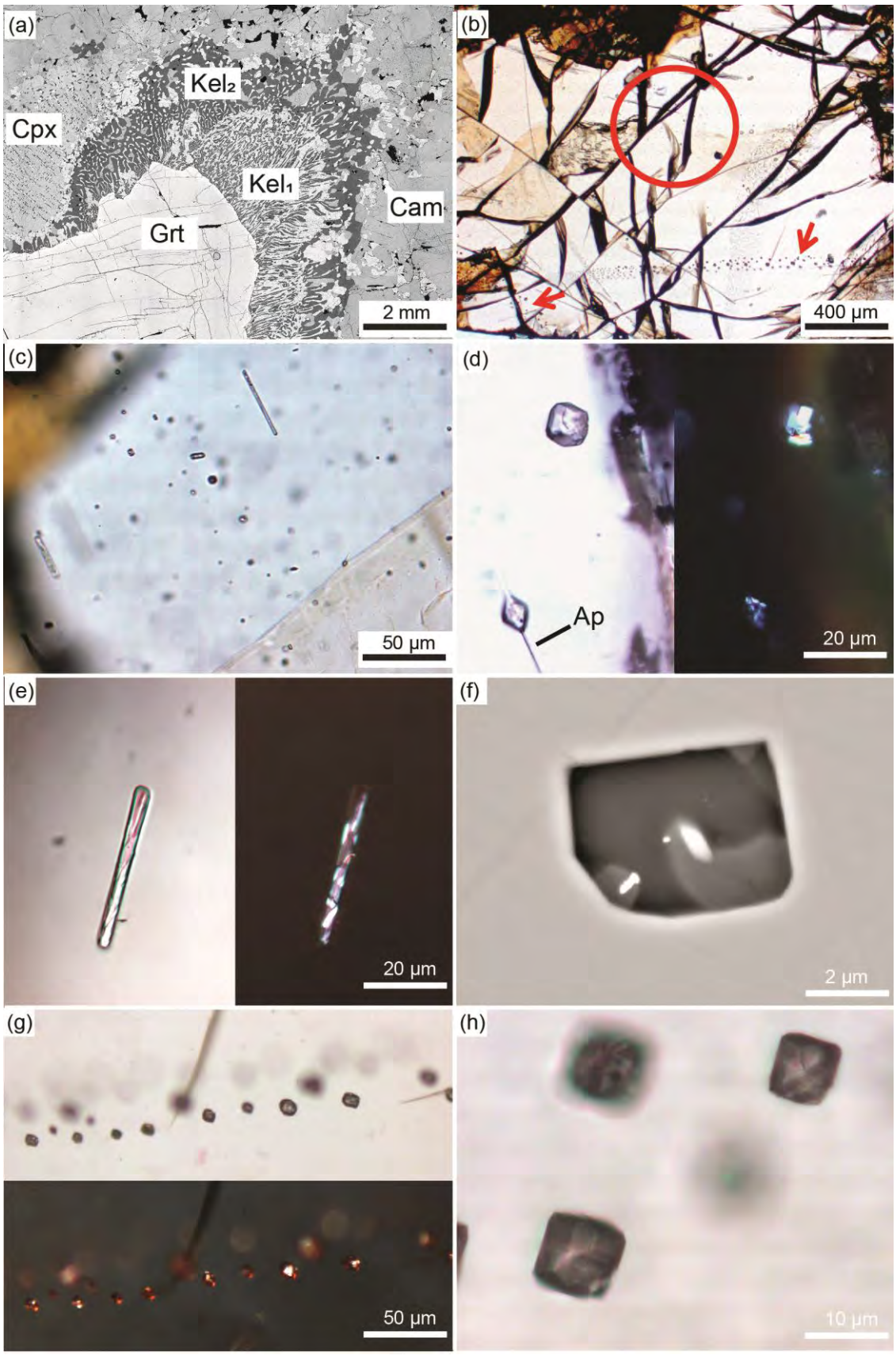

Fig. 2

This is a preprint, the final version is subject to change, of the American Mineralogist (MSA)
Cite as Authors (Year) Title. American Mineralogist, in press.
DOI: https://doi.org/10.2138/am-2018-6214

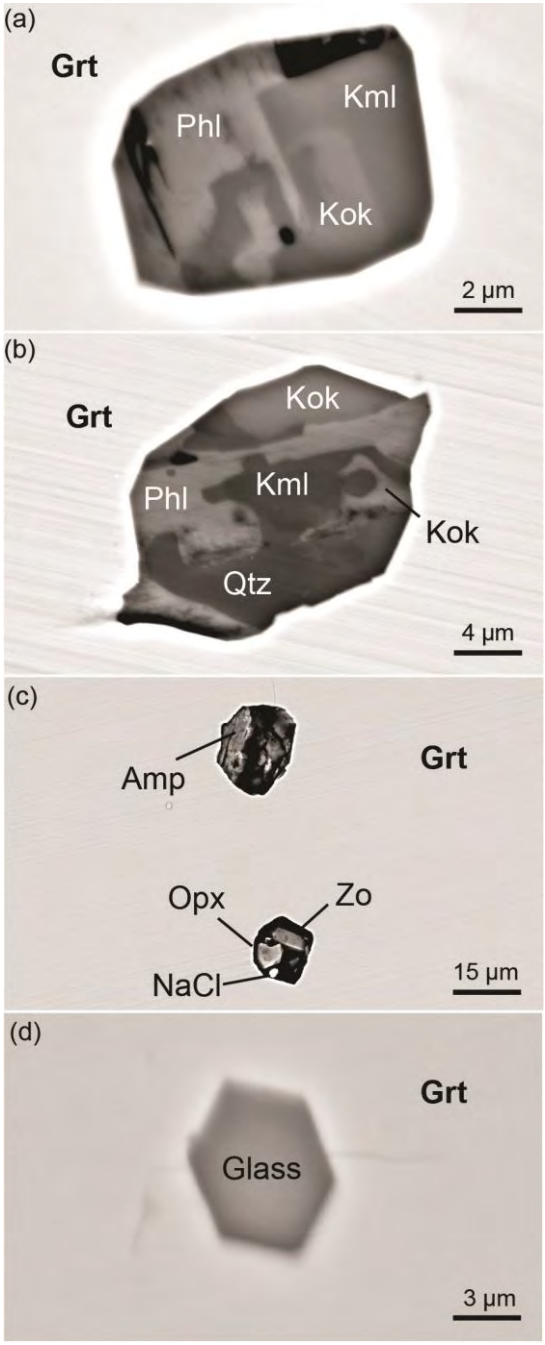

898

899 Fig. 3

900

This is a preprint, the final version is subject to change, of the American Mineralogist (MSA)
Cite as Authors (Year) Title. American Mineralogist, in press.
DOI: https://doi.org/10.2138/am-2018-6214

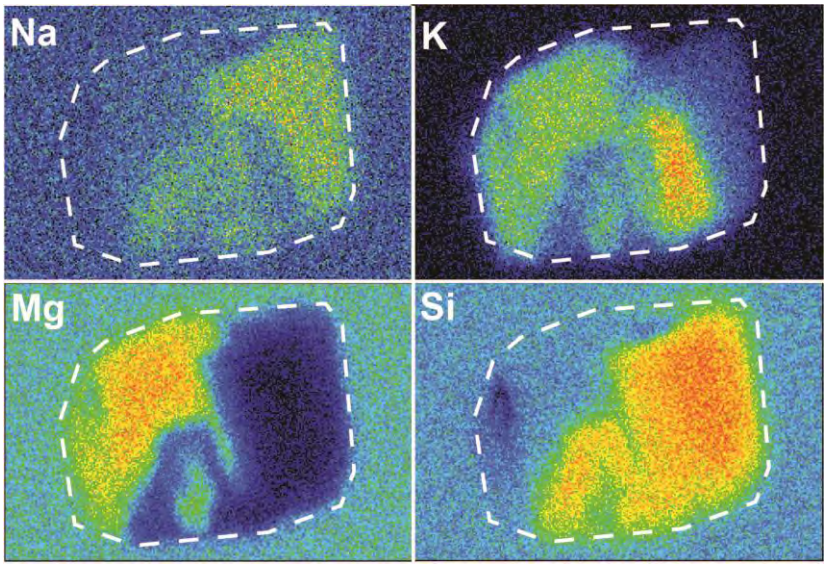

Fig. 4

This is a preprint, the final version is subject to change, of the American Mineralogist (MSA)
Cite as Authors (Year) Title. American Mineralogist, in press.
DOI: https://doi.org/10.2138/am-2018-6214

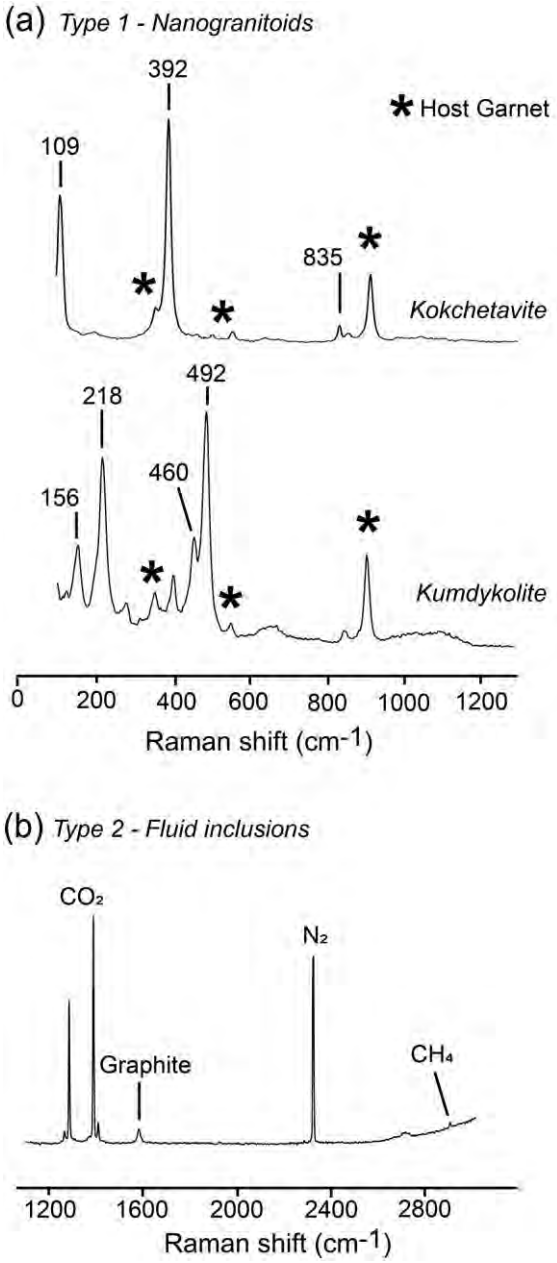

Fig. 5

This is a preprint, the final version is subject to change, of the American Mineralogist (MSA)
Cite as Authors (Year) Title. American Mineralogist, in press.
DOI: https://doi.org/10.2138/am-2018-6214

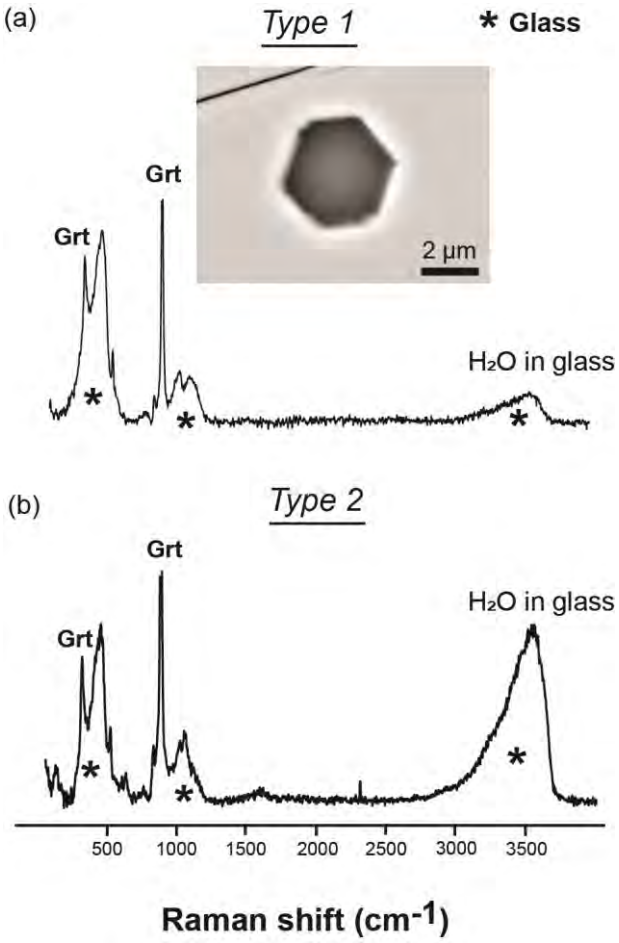

907

908 Fig.6

909

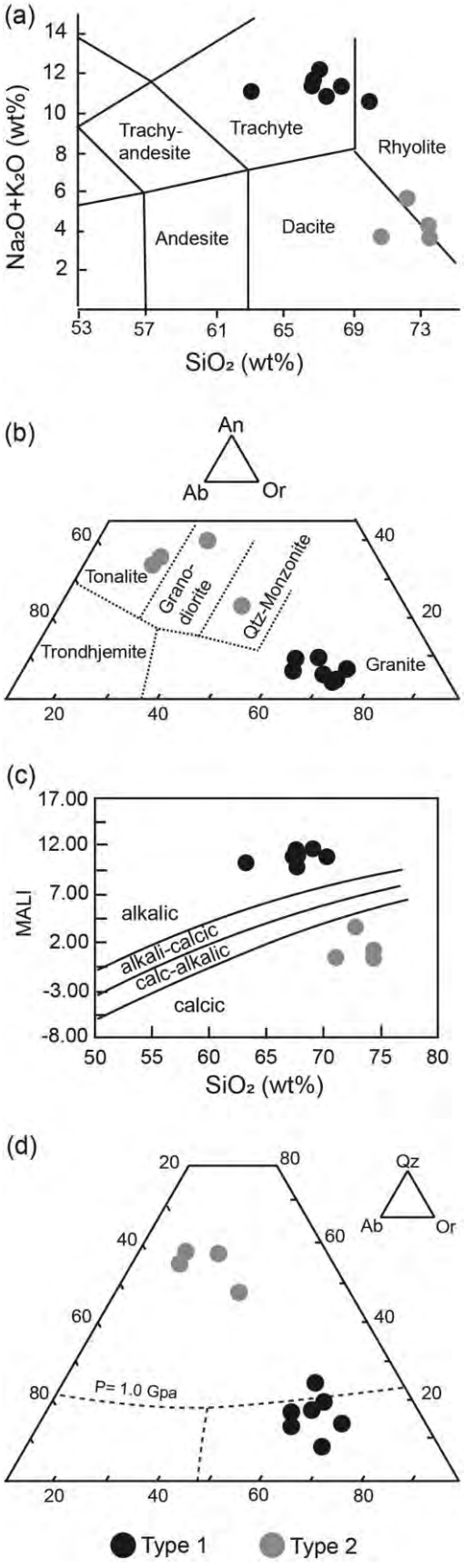

Fig. 7

This is a preprint, the final version is subject to change, of the American Mineralogist (MSA)
Cite as Authors (Year) Title. American Mineralogist, in press.
DOI: https://doi.org/10.2138/am-2018-6214

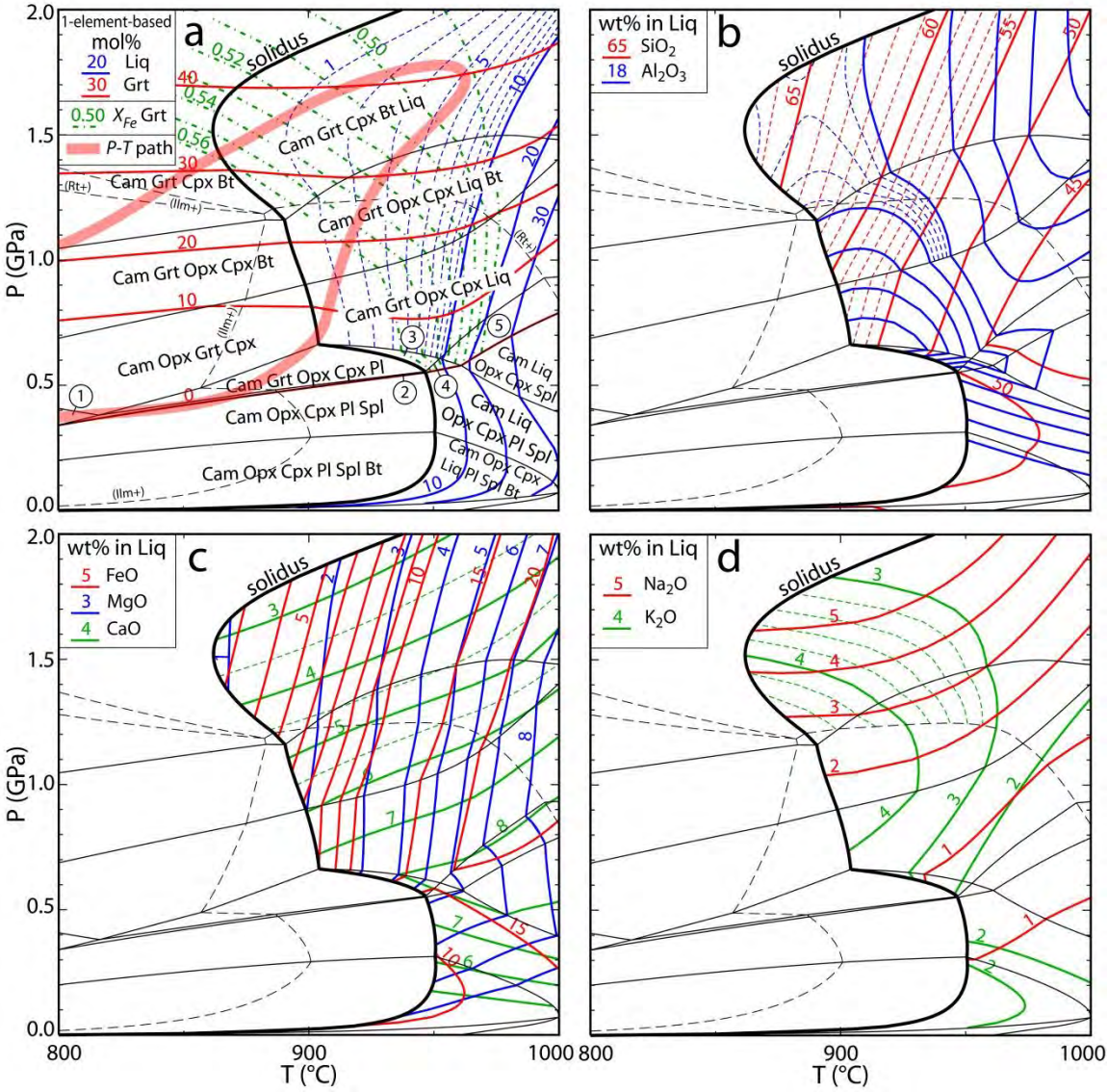

913

914 Fig. 8

915

This is a preprint, the final version is subject to change, of the American Mineralogist (MSA)
Cite as Authors (Year) Title. American Mineralogist, in press.
DOI: https://doi.org/10.2138/am-2018-6214

wt%	Amphibole av. EMPA	Grt core av. EMPA	Cpx scan EMPA	Bulk rock
SiO_2	41.59	39.49	49.25	44.29
TiO_2	1.97	0.05	0.45	0.99
Al_2O_3	14.67	22.10	8.07	15.61
Cr_2O_3	0.03	0.02	0.01	
FeO_T	10.83	20.14	8.95	12.81
MnO	0.11	0.42	0.15	0.19
MgO	13.20	11.77	12.97	13.74
CaO	11.57	6.08	18.72	10.06
Na_2O	2.12	n.d.	0.34	1.04
K_2O	1.61	n.d.	0.08	0.87
H_2O*	2.04	0.00	0.00	n.d.
Total	99.74	100.13	99.00	99.62
Si	6.115	2.973	1.837	27.439
Ti	0.218	0.003	0.013	0.463
Al	2.543	1.961	0.355	11.348
Cr	0.004	0.001	0.000	n.d.
Fe^{3+*}	0.000	0.035	0.000	n.d.
Fe^{2+}	1.332	1.233	0.279	6.639
Mn	0.014	0.026	0.005	0.098
Mg	2.893	1.321	0.721	12.690
Ca	1.823	0.490	0.748	6.678
Na	0.605	n.d.	0.025	1.249
K	0.301	n.d.	0.004	0.688
$\Sigma_{cations}$	15.847	8.043	3.987	67.352
O	22	12	8	100
OH*	2	0	0	n.d.
X_{Mg}	0.685	0.512	0.717	0.653

Table 1

This is a preprint, the final version is subject to change, of the American Mineralogist (MSA)
Cite as Authors (Year) Title. American Mineralogist, in press.
DOI: https://doi.org/10.2138/am-2018-6214

	EXPERIMENTAL PARAMETERS			RESULTS (Type-1 and Type-2)	
Name	Temperature (°C)	Pressure (GPa)	Duration (h)	Incomplete re-melting	Re-homogenization
1	950	22	24	-	X
2	900	22	24	X	-
3	950	24	24	-	X
4	950	15	24	-	X

Table 2

	Type 1								Type 2				
Wt%	*Gl.*	*2*	*11*	*M1*	*4*	*3*	*1_2*	**Av.**	*1*	*2*	*3*	*24*	**Av.**
SiO_2	67.02	66.93	64.82	64.21	69.21	67.37	60.15	**65.67**	65.66	64.62	62.33	62.73	**63.84**
TiO_2	0.00	0.09	0.22	0.04	0.05	0.06	0.11	**0.08**	0.08	0.03	0.24	0.03	**0.09**
Al_2O_3	15.85	17.26	16.90	16.44	17.38	17.28	17.92	**17.00**	12.11	12.26	13.64	12.29	**12.57**
FeO	1.16	1.43	1.34	1.40	0.98	1.70	2.28	**1.47**	2.68	2.64	2.56	2.80	**2.67**
MnO	0.00	0.04	0.00	0.00	0.02	0.09	0.07	**0.03**	0.02	0.00	0.00	0.07	**0.02**
MgO	0.34	0.88	0.67	0.74	0.41	0.95	2.86	**0.98**	1.03	1.11	2.37	0.73	**1.31**
CaO	0.72	1.37	1.18	1.06	0.90	1.08	1.68	**1.14**	3.03	2.97	3.21	2.38	**2.89**
Na_2O	1.95	2.90	3.05	1.86	2.21	2.37	2.35	**2.38**	2.52	2.26	1.62	1.90	**2.07**
K_2O	8.07	7.81	8.04	9.34	9.18	8.45	8.28	**8.45**	1.09	1.07	1.62	3.06	**1.71**
P_2O_5	0.00	0.00	0.00	0.00	0.06	0.02	0.00	**0.01**	0.14	0.06	0.00	0.17	**0.09**
Total	95.11	98.70	96.22	95.08	100.41	99.36	95.69	**97.22**	88.36	86.99	87.59	86.15	**87.27**
Q	22	15	12	13	18	16	5	**14**	37	37	34	32	**34**
C	3	2	1	1	2	2	2	**2**	2	2	3	2	**2**
Or	48	46	47	55	54	50	49	**50**	6	6	10	18	**14**
Ab	17	25	26	16	19	20	20	**20**	21	19	14	16	**17**
An	4	7	6	5	4	5	8	**6**	14	14	16	11	**12**
Hy	3	5	4	4	3	6	11	**5**	7	8	10	7	**8**
ASI	1.20	1.10	1.06	1.09	1.14	1.15	1.13	**1.12**	1.12	1.19	1.33	1.14	**1.17**
H_2O by diff	4.89	1.30	3.78	4.92	-0.41	0.64	4.31	**2.78**	11.64	13.01	12.41	13.85	**13.29**
Mg#	0.34	0.52	0.47	0.49	0.42	0.49	0.68	**0.54**	0.41	0.43	0.62	0.31	**0.40**
K_2O/Na_2O	4.14	2.7	2.63	5.0	4.16	3.57	3.53	**3.55**	0.43	0.47	1.00	1.61	**1.20**
K_2O/H_2O	1.65	6.02	2.13	1.90	-22.28	13.13	1.92	**3.05**	0.09	0.08	0.13	0.22	**0.18**

notes: Gl.= glassy inclusion; av.=average; n.d.= not determined

Table 3

This is a preprint, the final version is subject to change, of the American Mineralogist (MSA)
Cite as Authors (Year) Title. American Mineralogist, in press.
DOI: https://doi.org/10.2138/am-2018-6214

925

	Melt	Input parameters				Output parameters							
	n°	***P***	***T***	**H_2O**	**Bulk composition**	**Melt %**	**Melt composition (wt%, without H_2O)**						
		(GPa)	(°C)	**% (1)**	(2)	(mol)(3)	SiO_2	Al_2O_3	FeO	MgO	CaO	Na_2O	K_2O
MI	Type 1						**67.62**	**17.50**	**1.54**	**1.01**	**1.17**	**2.45**	**8.70**
Model	1	1.43	865	100	*1×TF4*	0.02	66.48	18.07	2.87	0.95	3.52	3.86	4.25
	2	1.45	870	100	*1×TF4*	0.24	66.06	18.12	3.11	1.04	3.49	4.03	4.14
	3	1.56	890	100	*1×TF4*	0.93	64.31	18.20	4.29	1.49	3.36	4.62	3.72
	4	1.66	910	100	*1×TF4*	1.40	62.44	18.01	5.85	2.07	3.28	5.01	3.34
	5	1.74	930	100	*1×TF4*	1.89	60.26	17.53	7.99	2.82	4.05	5.01	3.06
	6	1.45	870	100	*1×TF4*	0.24	66.06	18.12	3.11	1.04	3.49	4.03	4.14
	7	1.45	870	100	*0.98×TF4+0.02×MI*	4.09	66.11	18.18	3.08	1.01	3.53	3.95	4.21
	8	1.36	850	100	*0.99×TF4+0.01×MI*	1.07	67.64	17.87	2.24	0.71	3.70	3.25	4.59
	9	1.36	850	100	*0.98×TF4+0.02×MI*	2.86	67.65	17.89	2.22	0.70	3.72	3.22	4.60
	10	1.36	850	100	*0.97×TF4+0.03×MI*	4.62	67.65	17.90	2.21	0.70	3.73	3.20	4.62
	11	1.56	890	100	*1×TF4*	0.93	64.31	18.20	4.29	1.49	3.36	4.62	3.72
	12	1.56	890	99	*1×TF4*	0.23	66.63	17.86	2.86	0.99	2.92	4.74	3.99
	13	1.56	890	95	*1×TF4*	0.06	67.16	17.75	2.57	0.89	2.81	4.76	4.05
	14	1.43	865	100	*1×TF4; without Bt*	0.31	63.83	17.90	3.93	1.19	3.20	1.89	8.06

926

927 Table 4

928